International Journal of Nanomedicine

Dovepress
open access to scientific and medical research

Open Access Full Text Article

ORIGINAL RESEARCH

cRGD-Conjugated Fe_3O_4@PDA-DOX Multifunctional Nanocomposites for MRI and Antitumor Chemo-Photothermal Therapy

This article was published in the following Dove Press journal:
International Journal of Nanomedicine

Xi Fan,[1,2,*] Zeting Yuan,[1,*] Chenting Shou,[3,*] Guohua Fan,[1] Hong Wang,[2] Feng Gao,[3] Yuanpeng Rui,[4] Ke Xu,[1] Peihao Yin[1,2,5,6]

[1]Interventional Cancer Institute of Chinese Integrative Medicine, Putuo Hospital, Shanghai University of Traditional Chinese Medicine, Shanghai, People's Republic of China; [2]School of Medicine and Life Sciences, Chengdu University of Traditional Chinese Medicine, Chengdu, People's Republic of China; [3]Department of Pharmaceutics, School of Pharmacy, East China University of Science and Technology, Shanghai, People's Republic of China; [4]Department of Image, Putuo Hospital, Shanghai University of Traditional Chinese Medicine, Shanghai, People's Republic of China; [5]Department of General Surgery, Putuo Hospital, Shanghai University of Traditional Chinese Medicine, Shanghai, People's Republic of China; [6]Shanghai Putuo Central School of Clinical Medicine, Anhui Medical University, Anhui, People's Republic of China

*These authors contributed equally to this work

Correspondence: Peihao Yin
Department of General Surgery, Putuo Hospital, Shanghai University of Traditional Chinese Medicine, Shanghai, People's Republic of China
Tel +86-21-2223 3836
Fax +86-21-5266 5957
Email yinpeihao@shutcm.edu.cn

Ke Xu
Interventional Cancer Institute of Chinese Integrative Medicine, Putuo Hospital, Shanghai University of Traditional Chinese Medicine, Shanghai, People's Republic of China
Tel +86-21-2223 3222
Email kexu2577@shutcm.edu.cn

Background: Photothermal therapy (PTT) has great potential in the clinical treatment of tumors. However, most photothermal materials are difficult to apply due to their insufficient photothermal conversion efficiencies (PCEs), poor photostabilities and short circulation times. Furthermore, tumor recurrence is likely to occur using PTT only. In the present study, we prepared cyclo (Arg-Gly-Asp-d-Phe-Cys) [c(RGD)] conjugated doxorubicin (DOX)-loaded Fe_3O_4@polydopamine (PDA) nanoparticles to develop a multifunctional-targeted nanocomplex for integrated tumor diagnosis and treatment.

Materials and methods: Cytotoxicity of Fe_3O_4@PDA-PEG-cRGD-DOX against HCT-116 cells was determined by cck-8 assay. Cellular uptake was measured by confocal laser scanning microscope (CLSM). Pharmacokinetic performance of DOX was evaluated to compare the differences between free DOX and DOX in nanocarrier. Performance in magnetic resonance imaging (MRI) and antitumor activity of complex nanoparticles were evaluated in tumor-bearing nude mice.

Results: Fe_3O_4@PDA-PEG-cRGD-DOX has a particle size of 200–300 nm and a zeta potential of 22.7 mV. Further studies in vitro and in vivo demonstrated their excellent capacity to target tumor cells and promote drug internalization, and significantly higher cytotoxicity with respect to that seen in a control group was shown for the nanoparticles. In addition, they have good thermal stability, photothermal conversion efficiencies (PCEs) and pH responsiveness, releasing more DOX in a mildly acidic environment, which is very conducive to their chemotherapeutic effectiveness in the tumor microenvironment. Fe_3O_4@PDA-PEG-cRGD-DOX NPs were used in a subcutaneous xenograft tumor model of nude mouse HCT-116 cells showed clear signal contrast in T2-weighted images and effective anti-tumor chemo-photothermal therapy under NIR irradiation.

Conclusion: According to our results, Fe_3O_4@PDA-PEG-cRGD-DOX had a satisfactory antitumor effect on colon cancer in nude mice and could be further developed as a potential integrated platform for the diagnosis and treatment of cancer to improve its antitumor activity against colon cancer.

Keywords: Fe_3O_4 nanoparticles, polydopamine, cRGD, magnetic resonance imaging, MRI, chemo-photothermal therapy, tumor target

Introduction

Colon cancer carries a serious risk for morbidity and mortality among the various cancers.[1] Many clinical methods, such as surgery, radiotherapy and chemotherapy, have been utilized to treat colon cancer.[2–4] These methods, however, when clinically applied, have several shortcomings, and disease recurrence, metastasis, and destruction

of normal tissue cells and the immune system may occur.[5,6] Near-infrared ray (NIR)-mediated photothermal therapy (PTT) is a promising treatment method. PTT utilizes photothermal transduction agents (PTAs) to convert optical energy into thermal energy, thus killing cancer cells.[7–10] PTT is highly targeted, highly effective, minimally invasive, and has few side effects, and can thus be used for the treatment of various types of cancer.[11] In particular, nano-PTAs have high PCEs and accumulate well in tumor regions because of the enhanced permeability and retention (EPR) effect.[12–15] However, the use of PTT alone has constraints, such as a limited light-penetration depth, which may lead to incomplete elimination of cancer cells, and residual cells at the edges of a treated area can become a latent cause of recurrence and metastasis.[16] Therefore, it seems necessary and more promising to combine PTT with other therapies, and the resulting effect can not only be additive but also synergistic. PTT can kill cancer cells by improving the efficiency of drug delivery, regulating drug release, regulating the tumor microenvironment, inducing specific antigen release, or influencing other biologically related reactions.[17,18] For example, combined PTT and chemotherapy can circumvent drug resistance, reduce side effects, and achieve spatiotemporal drug release.[19–23]

Superparamagnetic iron oxide nanoparticles (Fe_3O_4 core diameter, ≤20 nm) have unique magnetic responsiveness and photothermal effects,[24–26] and hence can be utilized in PTT and MRI, which have received much attention as tools for the diagnosis and treatment of tumors.[27] Previous studies have shown that Fe_3O_4 has a strong *T*2 relaxation signal, making it a preferred nanomaterial among MRI contrast agents.[6] Therefore, Fe_3O_4 nanoparticles have been successfully developed into an MRI contrast agent and proven to be safe for humans.[28–30] Moreover, Fe_3O_4 absorption by the body is accompanied by efficient biodegradation and iron homeostasis mechanisms for treating the free ions.[31,32] However, Fe_3O_4 nanoparticles require appropriate surface functionalization to prevent them from being cleared from the circulatory system by the immune system.

According to recent studies, Polydopamine (PDA) is a strong NIR absorber and has a high PCE (40%).[33] PDA nanoparticles can be produced by self-polymerization, and their biocompatibility and PCE are greater than those of gold nanorods, reflecting their appreciable clinical application potential.[34] In addition, PDA films can be easily deposited onto a variety of inorganic and organic materials, and the functional groups (catechol and amine) on their surfaces are able to interact with other molecules.[35,36] Studies have shown that PDA can function synergistically with Fe_3O_4 to enhance photothermal effects and reduce laser power requirements.[37]

Integrins are cell-surface transmembrane receptors that participate in adhesion interactions in the process of transfer cascades, and they have been shown to be overexpressed in various cancers. Studies have shown that $\alpha_V\beta_3$ integrins are ideal biomarkers for colon cancer.[37,38] Integrins bind to ligands by identifying a sequence of amino acids (Arg-Gly-Asp, RGD) on the ligand. RGD is the most common recognition site for most integrin-binding ligands. However, different RGD peptides have different affinities for integrin subtypes. In particular, cyclic RGD peptides have been shown to exhibit improved affinity, receptor selectivity, and enzymatic stability, relative to linear peptides.[39–43]

In this study, we presented a multifunctional targeting nanocomplex integrating tumor diagnosis and treatment. After spectroscopic verification of the successful synthesis of these Fe_3O_4@PDA-PEG-cRGD-DOX NPs, we carried out PCE tests as well as in vitro test of the cellular toxicity, DOX release, and cellular uptake. We also examined the NPs in vivo, as an MRI contrast agent, and their therapeutic effect in vivo. We believe that our study makes a significant contribution to the literature because we were able to show that the Fe_3O_4 @PDA-PEG-cRGD-DOX NPs have good biocompatibility and excellent photothermal conversion ability, and can significantly suppress the proliferation of cells in vitro via a synergistic effect, combining DOX chemotherapy and PTT. We also investigated the pharmacokinetics of NPs-loaded DOX in rats, which showed superior long circulation in vivo. Thanks in part to their enhanced effectiveness under acidic conditions, in vivo experiments showed that the NPs could effectively target tumor tissues via to EPR and active targeting effects and that they can significantly inhibit tumor growth under NIR irradiation, as well as the fact that they have excellent contrast for MRI imaging. This particular NPs presented have not previously been prepared and have not previously been tested for use as an integrated therapy and diagnostic nanosystem. Therefore, we believe that this nanoparticle system has excellent prospects for development as a new integrated imaging, chemotherapy, and PTT agent to aid in the diagnosis and treatment of cancers.

Materials and Methods

Materials

Dopamine hydrochloride (DA·HCl) was purchased from Adamas Reagent, Ltd. (Shanghai, China), trimethylaminomethane (>99.0%, AR) and hydrochloric acid (36~38%, AR)

were purchased from Nanjing Chemical Reagent Company Ltd. (Nanjing, China), and nanometer iron tetroxide dispersion (25% in H_2O, 10~30nm) was obtained from Macklin Inc. (Shanghai, China). NH_2-PEG_{5000}-Mal (molecular weight 5000, purity 95%) was obtained from Shanghai maokang biological technology co., Ltd. (Shanghai, China), anhydrous sodium acetate (content >99.0%, AR) and acetic acid (content 99.5%, AR) were acquired from Shanghai Lingfeng Chemical Reagent co., Ltd. (Shanghai, China). cRGD was obtained from Nanjing peptide biotechnology co., Ltd. (Nanjing, China), NH_2-PEG_{5000} was procured from Shanghai Yare Biotech, Inc. (Shanghai, China), and doxorubicin hydrochloride (DOX·HCl) (purity >99%) was obtained from Sigma-Aldrich Chemical Co. (St Louis, MO, USA).

AL104 electronic balance was provided by mettler Toledo instruments co., Ltd. (Shanghai, China), B11-3 thermostatic magnetic stirrer was offered by Shanghai sile instruments co., Ltd. (Shanghai, China), Pennsylvania-based firm Zetasizer Nano ZS90 Nano particle and Zeta voltmeter was purchased from British melvin instrument co., Ltd. (UK), GL–18B centrifuge table high speed was obtained from Shanghai medical equipment co., Ltd. Surgical instrument factory (Shanghai, China), and micro quantitative pipette was offered by dragon medical equipment co., Ltd. (Shanghai, China), XW–80A vortex mixer was offered by Shanghai jingke industrial co., Ltd. (Shanghai, China). Xingzhi biotechnology co., Ltd. provided SB-4200 type NC ultrasonic cleaners (Ningbo, China), Shanghai Billon instrument co., Ltd. provided BILON92-DL cell disruptor (Shanghai, China), and Dialysis bag (Mw=3500 Da) was purchased from Shanghai yuanye biotechnology co., Ltd. (Shanghai, China), SHA-CA digital display water bath thermostatic oscillator was obtained from Union instrument institute (Jiangsu, China).

Cells and Animals

The Shanghai Institute for Biological Sciences (Shanghai, China) provided HCT-116cells, which were hatched in RPMI-1640 containing 10% fetal bovine serum (FBS) under proper conditions (37°C, 5% CO_2, humidity of 95%). RPMI-1640 and FBS were obtained from Invitrogen (Carlsbad, CA, USA) and used as received. The water used in all experiments was ultrapure, produced by a Milli-Q water purification system from Millipore (France).

Nude mice (male, 4–5weeks old, weight 20 ± 2 g) were obtained from the Shanghai Laboratory Animal Center, Chinese Academy of Medical Sciences (Shanghai, China). All animals were housed under SPF conditions in the laboratory animal facility in Putuo hospital, Shanghai university of Traditional Chinese medicine. The mice lived in the environment with a relative humidity of 60±10%, noise level lower than 55 dB, and at the temperature of 25 ±3°C. All procedures were performed under the approval of the Administrative Panel on Laboratory Animal Care of the Putuo District Center Hospital. All animals received care following the guidelines outlined in the "Laboratory Animal-Guideline for ethical review for animal welfare."

Methods

Synthesis of Fe_3O_4@PDA NPs

10 mg of DA·HCl was accurately weighed and dissolved in Tris buffer (50 mL, 10 mM, pH 8.5). 20 μl of Fe_3O_4 NP dispersion (1 mg/μL) was added drop by drop. At room temperature, we used a magnetic stirrer to stir the liquid in the dark for 8 hrs at a speed of 800 rpm. At the end of the reaction, the supernatant was centrifuged with a frozen high-speed centrifuge for 15 mins at a speed of 12,000 rpm and then was discarded carefully. Remove the lower precipitate and re-centrifuge with the deionized water for three times. Finally, 10 mL deionized water was added to redissolve, and we got the Fe_3O_4@PDA dispersion liquid.

Synthesis of Fe_3O_4@PDA-DOX NPs

125 μL DOX·HCl aqueous solution was added into Fe_3O_4 @PDA dispersion liquid (5 mL) drop by drop. At room temperature, the mixed liquid above was stirred by magnetic force for 12 hrs in the dark at the speed of 800 rpm. At the end of the reaction, the supernatant was centrifuged with a frozen high-speed centrifuge for 15 mins at a speed of 12,000 rpm and then was discarded carefully. Remove the lower precipitate and re-centrifuge with the deionized water for three times. At last, 5 mL of deionized water was added to redissolve and we got the Fe_3O_4@PDA-DOX dispersion liquid.

Synthesis of Fe_3O_4@PDA-PEG-cRGD-DOX NPs

40 mg NH_2-PEG_{5000}-Mal was weighed and dissolved in NaAc-Hac buffer (1 mL, pH 6) exposuring in ultrasound for 5 mins. 10 mg cRGD powder was weighed and dissolved in 1 mL NaAc-Hac buffer (pH=6) exposuring in ultrasound for 5 mins to obtain 10 mg/mL cRGD solution. 0.4 mL of cRGD solution (10 mg/mL) was added into NH_2 -PEG_{5000}-Mal solution drop by drop and oscillated in

a constant temperature water bath for 24 hrs (170 r/min). After the reaction, hemodialysis was performed for 48 hrs (the molecular weight was retained for 3500 Da, and the fluid was changed for 6 times). The dialysate was freeze-dried and verified by ^{1}H NMR. Tris solution of Fe_3O_4 @PDA NPs (10 mL, 1 mg/mL) and NH_2-PEG-cRGD aqueous solution (400 μL, 5 mg/mL) were added to NH_2-PEG_{5000} (20 mg), respectively, and then avoid light for 24 hrs. The reaction liquid above was centrifuged and washed with Tris for 3 times and then verified by Fourier transform infrared spectroscopy (FTIR). 5 mL of the above Fe_3O_4@PDA-PEG-cRGD product was added to 250 μL DOX·HCl aqueous solution, and the reaction was conducted in dark for 12 hrs. The reaction liquid above was centrifuged and washed with Tris for 3 times. And end up with a freeze-dried solid of 12.5 mg.

The content of DOX was detected by an enzyme marker and the drug loading rate (LE) was calculated with the formula below:

$$LE = \text{Drugs in the carrier/added drugs} \times 100\%$$

Characterization

The nanoparticles' size and potential were measured by laser granularity analyzer. The nanoparticles' morphology was characterized by transmission electron microscopy (TEM). The structure of nanoparticles was characterized by XPS and FTIR. UV-vis-NIR absorption spectrum was obtained on a Lambda UV-3300 spectrophotometer.

In vitro DOX Release

Fe_3O_4@PDA-PEG-cRGD-DOX NPs (1 mg/mL) was added into the dialysis bag (Mw = 3500 Da) to investigate its release in PBS solutions with different pH (pH 5.0, pH 7.4). In the control group, Fe_3O_4@PDA-PEG-cRGD-DOX NPs was added into the dialysis bag (Mw = 3500 Da) illuminated with NIR (808 nm, 1 W/cm^2) at different time points (2 hrs, 4 hrs, 8 hrs, 12 hrs, 18 hrs, 24 hrs) for 5 mins. The liquid of all groups were sampled at these time points (0 mins, 10 mins, 30 mins, 1 hrs, 2 hrs, 4 hrs, 8 hrs, 12 hrs, 18 hrs, 24 hrs) and tested DOX concentration by microplate reader (Thermo Fisher Scientific) to investigate the influence of pH and photothermy on DOX release.

In vitro Photothermal Effect and Stability

Different concentrations of Fe_3O_4@PDA-PEG-cRGD-DOX NPs (0, 25, 50, 100, and 200 μg/mL) were treated by 808-nm wavelength illumination (1 W/cm^2) for 5 mins. The temperature of the solution was measured every 1 min using a temperature-sensitive probe to investigate the photothermal effect of the NPs. When the temperature had no longer increased, we turned down the NIR and left the temperature return to room temperature which was considered as a cycle. Five cycles will be conducted, and the temperature will be recorded every 1 min.

In vitro and in vivo MRI

Different concentrations of Fe_3O_4@PDA-PEG-cRGD-DOX NPs (0, 0.2, 0.4, 0.6, 0.8, and 1.0 μg/mL) were placed in an eppendorf tube (1.5 mL) with vortexing for 3 mins. And the samples were imaged by 3.0 T magnetic resonance instrument (TR: 1,100.0 ms; TE: 28.7 ms, field of view, 150 × 250 mm; and slice, 2.5 mm).

In vivo imaging studies were performed when the tumor volume was reached 800 mm^3. We injected Fe_3O_4 @PDA-PEG-cRGD-DOX NP solution (100 μL, 500 μg/mL) into the tumed-bearing mice by tail vein, and conducted MRI of the mice at different times (0 hrs, 12 hrs, 24 hrs) with 3.0 T magnetic resonance instrument (TR: 1,800.0 ms; TE: 43.2 ms, field of view, 50 × 90 mm; and slice, 2.5 mm).

Cell Uptake Experiment

In the irradiation-free group, HCT-116 cells were, respectively, incubated with Fe_3O_4@PDA-DOX and Fe_3O_4 @PDA-PEG-cRGD-DOX NPs for 2, 6, 12 and 24 hrs. The cells, fixed with 4% paraformaldehyde and then stained with DAPI, were observed by laser confocal microscopy.

In the irradiation group, Fe_3O_4@PDA-PEG-cRGD-DOX NPs was added to HCT-116 cells and incubated for 2 hrs, then subjected to NIR illumination (808 nm, 1W/cm^2) for 5 mins observed by laser confocal microscopy.

In addition, for proving the cRGD targeting to HCT-116 cells, HCT-116 cells were preincubated for 1 hr with free cRGD (0.3μg/mL) before treated with Fe_3O_4@PDA-PEG-cRGD-DOX NPs and then observed by CLSM after another 2 hrs of co-culturing.

In vitro Cytotoxicity

The cytotoxicity of Fe_3O_4@PDA NPs, Fe_3O_4@PDA-DOX NPs, Fe_3O_4@PDA-PEG-cRGD NPs and Fe_3O_4@PDA-PEG-cRGD-DOX NPs with NIR illumination or not, against HCT-116 cells were assessed by CCK-8 assay purchased from Dojindo (Kumamoto, Japan). HCT-116 cells were seeded into 96-well plates (1 × 10^6 cells/well) and

cultured for 24 hrs. Then, cells were treated with PBS, and different concentrations of Fe_3O_4@PDA NPs, Fe_3O_4@PDA-DOX NPs, Fe_3O_4@PDA-PEG-cRGD NPs and Fe_3O_4@PDA-PEG-cRGD-DOX NPs (concentration gradient of each were 6.25, 12.5, 25, 50, 100 and 200 μg/mL). Five hrs after adding the drug, the culture medium was removed and replaced with PBS, followed by NIR illumination (808 nm, 1W/cm^2) for 5 mins. After that, the fresh culture medium was put in again and the cells were incubated for another 24 hrs. At last, the culture medium was removed and 100 μL CCK-8 assay (10%) was added into each well and cultured for an additional 1.5 hrs. The absorbance was measured by a multifunctional microplate reader at 450 nm. The viability of the blank control group (PBS) was considered as 100%.

In vivo Pharmacokinetics

Six male SD rats (about 200 g) were randomly divided into two groups (n=3), followed by tail-vein injection of free DOX and Fe_3O_4@PDA-PEG-cRGD-DOX NPs with doses of 1.5 mg/kg. Blood sample (300 μL) was taken from the eye socket of the SD rats at different times (10, 15, 30, 60, 120, 240, 480, 1440 mins) followed by a high-speed cryogenic centrifugation (15,000 rpm, 10 mins). After accurately moving the upper plasma samples of 100 μL, DOX internal standard liquid and leaching liquor were added to each sample successively followed by being vibrated on the vortex for 5 min and then treated with high-speed cryogenic centrifugation (15,000 rpm, 10 mins). Finally, the organic phase was collected for HPLC detection. During blood collection, rats should properly supplement normal saline.

In vivo Evaluation of Antitumor Activity

To determine the antitumor effect of Fe_3O_4@PDA-PEG-cRGD-DOX NPs in vivo, we established a subcutaneous xenograft model in nude mice. Firstly, two nude mice were randomly picked out and injected with HCT-116 cells (5×10^6/mL) into the right flank region. When the tumor volume grew to about 200 mm^3, the tumors were removed and evenly divided into sections (volume=2×2×1 mm^3). Then, we transplanted the sections to others in the same region. When the average volume of transplanted tumor reached 150–200 mm^3, mice were randomly divided into eight groups (6 mice/group): normal saline group (Control), saline + NIR, Fe_3O_4@PDA NP, Fe_3O_4@PDA NP + NIR, Fe_3O_4@PDA-DOX NP, Fe_3O_4@PDA-DOX NP + NIR, Fe_3O_4@PDA-PEG-cRGD-DOX NP, Fe_3O_4@PDA-PEG-cRGD-DOX NP + NIR. Nanoparticle dispersions (100μg/mL, 100 μL) were injected into each group via tail vein. After 24 hrs of co-culturing, NIR (808 nm, 1W/cm^2) was performed for 5 mins. The tumors' size and mice weight were recorded every 4 days. The volume of tumors was calculated by the formula: Volume = π/6 ×length × width^2. On the 32nd day, the mice were executed. The heart, liver, spleen, lung, kidney and tumor tissues of these mice were taken out and prepared into pathological sections. H&E staining was used to observe the toxicity of nanoparticles of tissues in each group.

Statistical Analysis

Graph Pad Prism 5.0 software was used for statistical analysis. The main pharmacokinetic parameters were calculated using kinetica5.1. Experimental data were presented as mean ± standard deviation. Student's unpaired *t*-test was utilized to analyze the difference between groups. P-values under 0.05 were supposed to be significant.

Results and Discussion

Preparation and Characterization

Fe_3O_4@PDA-PEG-cRGD-DOX NP preparation method is shown schematically in Figure 1. Fe_3O_4@PDA NPs were prepared in an alkaline aqueous solution of Fe_3O_4 nanoparticles by self-aggregation of DA. As was apparent in the TEM image (Figure 2A and B), the Fe_3O_4@PDA NPs had a dispersed spherical shape and core-shell structure.

The ^{1}H NMR spectrum of NH_2-PEG_{5000}-cRGD was shown in Figure 2C. It was clear that after the reaction of cRGD and NH_2-PEG_{5000}-MAL to produce this material, the characteristic peak of the maleimide group (–MAL) (chemical shift, 6.8 ppm) was absent from the spectrum, and the cRGD characteristic peak (chemical shift, 7.2 ppm) was instead present. This result indicated the successful synthesis of NH_2-PEG_{5000}-cRGD NPs.

In Figure 2D, the peaks at 3421 cm^{-1} (N–H stretching vibration) and 1524 cm^{-1} (N–H bending vibration) in the infrared spectrum indicated that Fe_3O_4@PDA NPs were successfully synthesized. Then, the –NH2 and PDA underwent a Schiff base reaction, and the synthesized NH_2-PEG_{5000}-cRGD became attached to the surface of the Fe_3O_4@PDA NPs, introducing PEG and cRGD. Thus, the Fe_3O_4@PDA-PEG-cRGD NPs were obtained. The infrared spectrum of the Fe_3O_4@PDA-PEG-cRGD NPs had a peak at 1039 cm^{-1} (C–O–C stretching vibration), indicating the successful synthesis of the Fe_3O_4@PDA-PEG-cRGD NPs.

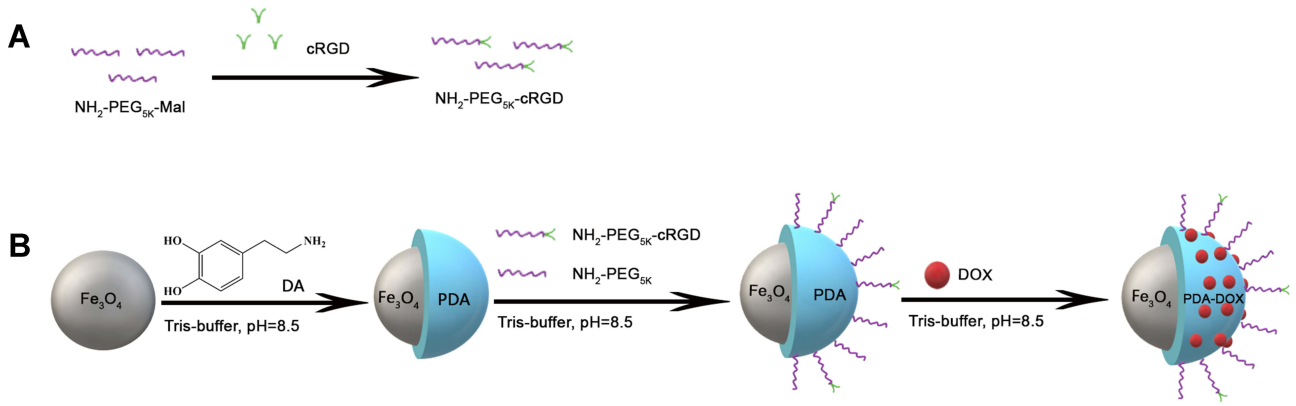

Figure 1 Schematic illustration of the synthesis of DOX-loaded Fe_3O_4@PDA-PEG-cRGD composite particles. (**A**) The junction of cRGD and PEG. (**B**) After the iron oxide core wrapped in the PDA, -PEG-cRGD was connected on the PDA.

Finally, DOX was adsorbed onto the surface of the nanoparticles by means of π–π conjugation between DOX and PDA, and the Fe_3O_4@PDA-PEG-cRGD-DOX NPs were thus prepared. DOX in supernatant and carrier were detected by a microplate reader, and drug LE was calculated to be 18.72%. Besides, through the results of UV-vis-NIR shown in Figure 2E, we could clearly see that the characteristic peak of DOX appeared in the absorption curve of Fe_3O_4@PDA-PEG-cRGD-DOX, indicating that DOX was loaded into the composite nanoparticles.

In Figure 2F and G, dynamic light scattering (DLS) showed that the Fe_3O_4@PDA-PEG-cRGD-DOX NPs had a final mean particle size of 275.4 nm and a mean zeta potential of 22.7 mV. In this range of sizes, phagocytosis by Kupffer cells was prevented and the chance of the nanoparticles being recognized and ingested by the reticuloendothelial system (RES) were reduced. Based on the EPR effect, the accumulation of the nanoparticles in the tumor region could facilitate passive targeting. In addition, the zeta potential could be used to characterize the stability of the colloidally dispersed system. Absolute values of the zeta potential of similar nanoparticles were greater than 20 mV, and hence a mutually repulsive force mediated the interaction between these nanoparticles and aggregation was disfavored; thus, they had a degree of stability.

Photothermal Properties

The photothermal conversion of the Fe_3O_4@PDA-PEG-cRGD-DOX NPs in an aqueous solution was achieved by irradiating them with NIR (808 nm, 1 W/cm^2). As shown in Figure 3, with increasing illumination time, the temperature increased significantly, and a concentration-dependent response was displayed. Notably, when the concentration of the Fe_3O_4@PDA-PEG-cRGD-DOX NPs was 200 μg/mL, the temperature increased to 45.5°C after 5 mins of irradiation, which was sufficient for killing tumor cells. The experimental data suggested that the PCE of these NPs was relatively high. To further analyze the photothermal stability of the NPs, the NP aqueous solution was irradiated with NIR (808nm, 1 W/cm^2) for 5 mins and then irradiated again for 5 mins after the temperature had returned to room temperature; this process was repeated for five cycles. The results showed that after five cycles the photothermal conversion ability of the Fe_3O_4@PDA-PEG-cRGD-DOX NPs did not drop. These results indicated that the Fe_3O_4@PDA-PEG-cRGD-DOX NPs had good photothermal conversion efficiency and photothermal stability. Thus, the NPs were suitable for use as PTT agents.

In vitro Cytotoxicity

The cytotoxicity of the NPs toward HCT-116 cells was evaluated by a CCK-8 assay. Figure 4 shows that the survival rate of the Fe_3O_4@PDA group (100 μg/mL) without light was 95.0%. Cell viability was 94.2% in the Fe_3O_4@PDA-PEG-cRGD group (100 μg/mL). The survival rate of the Fe_3O_4@PDA-DOX group (100 μg/mL) and Fe_3O_4@PDA-PEG-cRGD-DOX group (100 μg/mL) were 85% and 83.8%, respectively. All these abovementioned results indicated had good biocompatibility for the nanomaterials. After DOX loading, the toxicity of the nanomaterials increased slightly but remained within a safe range. As shown in Figure 4, the cell survival rate decreased significantly after NIR irradiation (808 nm, 1 W/cm^2 for 5 mins). The survival rate of the Fe_3O_4@PDA group (100 μg/mL), Fe_3O_4@PDA-DOX group (100 μg/mL) and Fe_3O_4@PDA-PEG-cRGD group (100 μg/mL) were 38.8%, 30.6% and 25.6%, respectively, and that of the Fe_3O_4@PDA-PEG-cRGD-DOX group

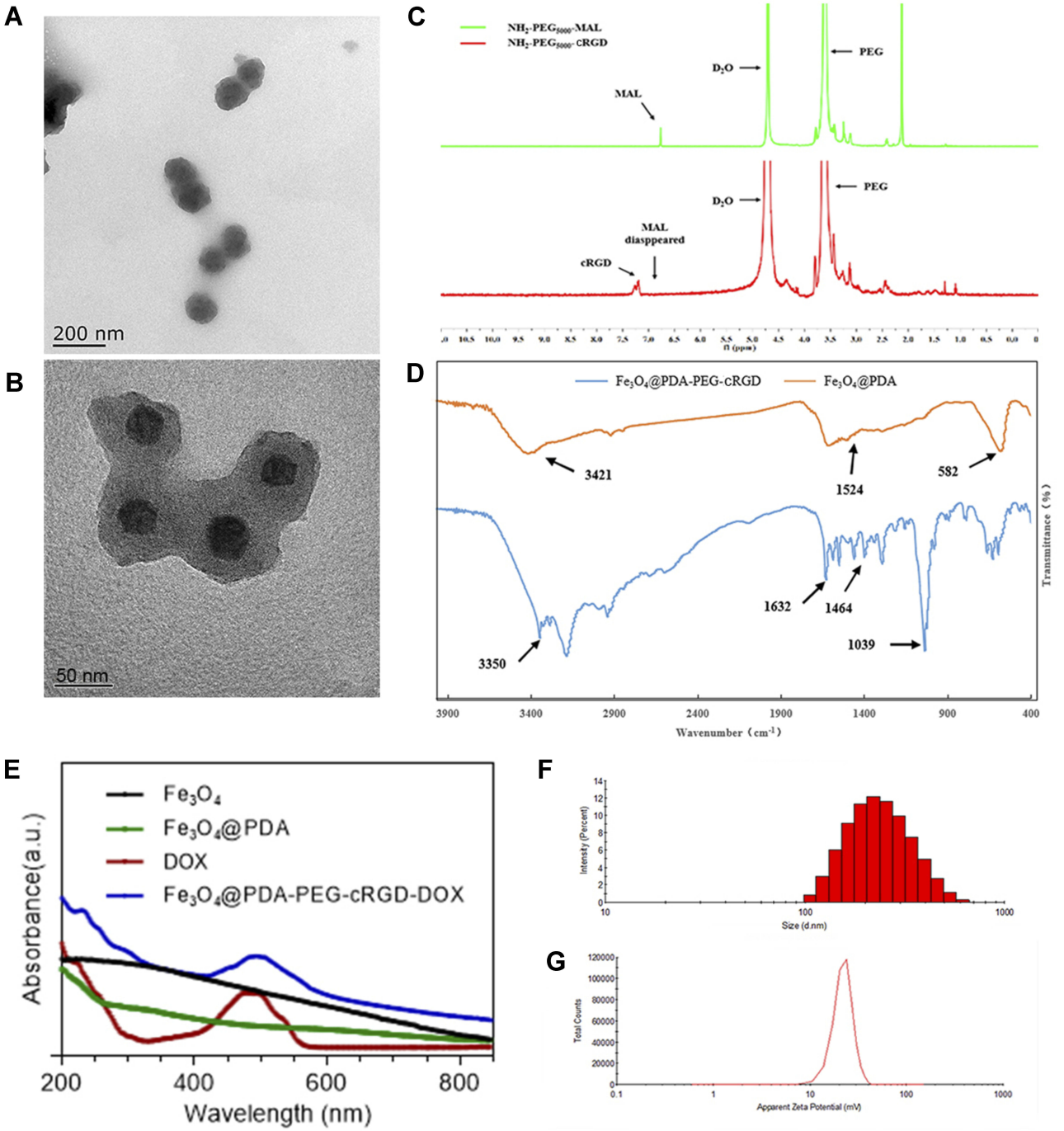

Figure 2 Characterization analysis of composite nanoparticles. (**A**) and (**B**) Showed the morphology of Fe_3O_4@PDA measured by TEM. (**C**) ^{1}HNMR of NH_2-PEG_{5000}-cRGD. (**D**) FTIR results of Fe_3O_4@PDA-PEG-cRGD and Fe_3O_4@PDA. (**E**) UV-vis-NIR absorption spectrum of different NPs. (**F**) Size distribution and (**G**) zeta potential distribution of Fe_3O_4@PDA-PEG-cRGD-DOX.

(100 μg/mL) was 22.4%. Compared to the untargeted group, the RGD-targeted nanoparticles increased the killing effect of the PTT, possibly because RGD could target the tumor cells and increased the cellular uptake of the photosensitizer and DOX. In summary, the cytotoxicity test results showed that the Fe_3O_4@PDA-PEG-cRGD nanomaterials had a strong killing effect on tumor cells under photothermal conditions, and the Fe_3O_4@PDA-PEG-cRGD-DOX nanomaterials had both a PTT effect and DOX chemotherapy effect, which synergistically exerted an antitumor effect.

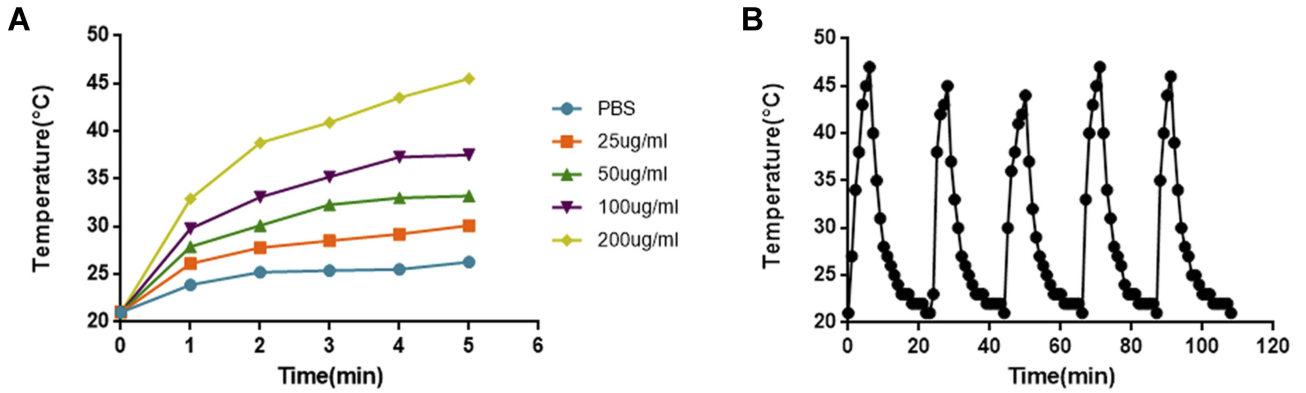

Figure 3 Photothermal effect and stability of Fe_3O_4@PDA-PEG-cRGD-DOX NPs. (**A**) Showed the increasing trend of temperature of Fe_3O_4@PDA-PEG-cRGD-DOX nanoparticles with different concentrations (PBS, 25μg/mL, 50μg/mL, 100μg/mL, 200μg/mL) under 808nm NIR irradiation. (**B**) Represented the photothermal stability of the same system (200 μL, 200μg/mL) with five consecutive photothermal cycles.

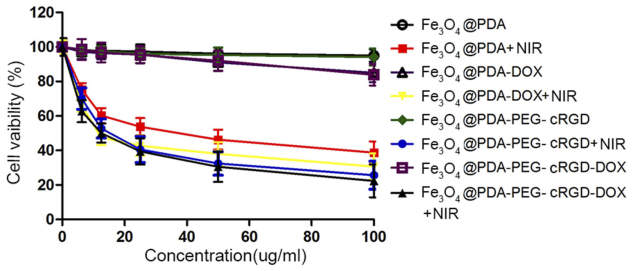

Figure 4 Cytotoxicity of composite nanoparticles on HCT-116 cells. The 24 hrs killing effects of Fe_3O_4@PDA, Fe_3O_4@PDA-DOX, Fe_3O_4@PDA-PEG-cRGD and Fe_3O_4@PDA-PEG-cRGD-DOX on HCT-116 cells under NIR irradiation or not. Data were represented as mean ± SD (n = 3).

Drug Release

We investigated the in vitro release of DOX from the Fe_3O_4@PDA-PEG-cRGD-DOX NPs in a buffer solution at pH 5.0 and pH 7.4 and under NIR irradiation (808 nm, 1 W/cm^2 for 5 mins). Figure 5A shows that after six rounds of NIR irradiation, 53.63% of the DOX is released from the NPs in the pH 7.4 buffer, while only 45.67% of the DOX is released in the pH 7.4 buffer without NIR irradiation. Thus, NIR irradiation accelerated the release of DOX from the NPs. Figure 5B shows that after six rounds of irradiation, 99.47% of the DOX was released from the NPs at pH 5.0; this compared well with the 53.63% value for the DOX released at pH 7.4 after the same irradiation treatment. Even in the absence of NIR irradiation, the amount of DOX released from the NPs at pH 5.0 (79.69%) was significantly higher than that released at pH 7.4 (45.67%). The reason for this pH dependence might be that under acidic conditions, NH_2 groups on the surface of PDA and DOX were protonated, and this affected the π–π bond interactions between PDA and DOX, making it easier to dissociate DOX from the NP surface. These results indicated that the NPs were stable under neutral conditions and were sensitive to pH. Furthermore, the NPs released DOX more readily under acidic conditions which should be beneficial for its release in the acidic microenvironments of tumors and specifically

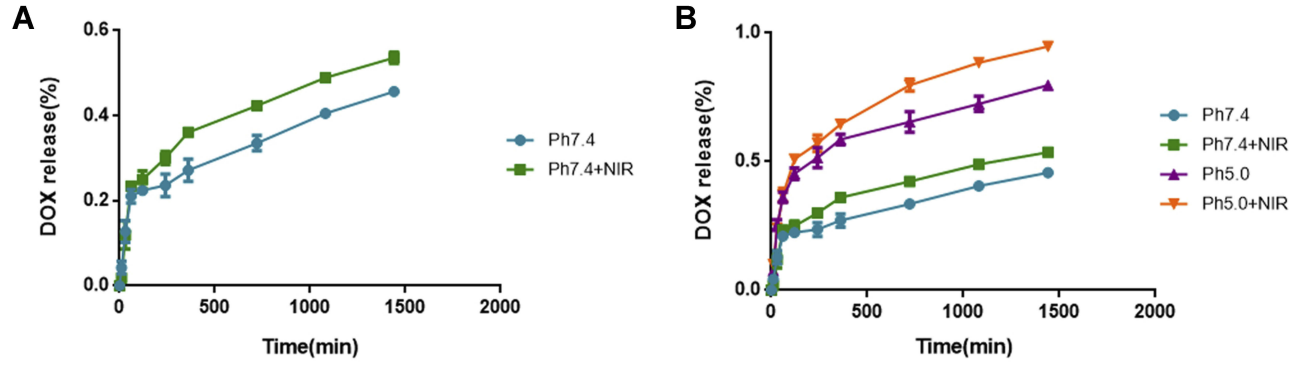

Figure 5 Drug-release profiles of Fe_3O_4@PDA-PEG-cRGD-DOX Nps at 37°C. (**A**) The effect of NIR illumination on the release of DOX from the NPs was investigated. (**B**) DOX release percentage from NPs at different PH (7.4, 5.0). The data are presented as the mean ± SD, n = 3.

of the lysosomes inside the tumor cells. It was also apparent, from these results, that NIR irradiation could be used to control the release rate of the drug.

Cellular Uptake

Cellular uptake of composite NPs was evaluated in HCT-116 cells by CLSM (Figure 6A), the NPs were mainly concentrated in the cytoplasm after cell uptake. In addition, it was clear from Figure 6B that the Fe_3O_4@PDA-PEG-cRGD-DOX NPs could increase cellular uptake of DOX compared to the Fe_3O_4@PDA-DOX NPs, reflecting the targeting effect of cRGD. However, free DOX was more readily absorbed by the cells than were the Fe_3O_4@PDA-PEG-cRGD-DOX NPs, and the subcellular distribution of DOX was mainly concentrated in the nucleus. This was because free DOX was a small-molecule drug with a positive charge that could easily diffuse across negatively charged cell membranes and into the nucleus. After 808-nm irradiation, the free DOX and NP fluorescence intensities were significantly higher than those of the unirradiated group, indicating that more NPs or drugs were absorbed by the cells owing to the PTT effect. If HCT-116 cells were preincubated with cRGD before treated with Fe_3O_4 @PDA-PEG-cRGD-DOX NPs, the DOX uptake rate was reduced, which might be due to the competitive binding of integrin to free ligands, demonstrating that cRGD can specifically target the receptors on HCT-116 cells to promote DOX entry into cells. The results of the cellular uptake experiments showed that PTT could not only increase the permeability of the cell membrane and increase the absorption of drugs but also accelerate the release of the NP-loaded drugs, and cRGD could target the tumor cells.

Magnetic Properties and in vivo MRI

A vibration sample magnetometer (VSM) was used to determine the magnetic properties of the Fe_3O_4@PDA-PEG-cRGD-DOX NPs. As shown in Figure 7A, it could be concluded from the magnetization curve that these NPs were superparamagnetic as there was no obvious remanence and coercivity at 300 K. The saturation magnetization (*M*s) values for the Fe_3O_4 NPs and Fe_3O_4@PDA-PEG-cRGD-DOX NPs were 77.879 and 52.681 emu/g, respectively. Although the value of the latter was significantly smaller, the magnetism was still very strong. Figure 7B shows two samples of the Fe_3O_4@PDA-PEG-cRGD-DOX composite particles with the same concentration, in which sample (A) particles were well dispersed in water, without a magnetic field while sample (B) particles were attracted to the sidewall by a magnet. After gentle shaking, the Fe_3O_4@PDA-PEG-cRGD-DOX composite particles could be uniformly re-dispersed in water within 30 s. In addition, the *T*2-weighted MR images (Figure 7C) showed that the contrast decreased with increasing Fe concentration. This indicated that the Fe_3O_4@PDA-PEG-cRGD-DOX NPs should prove to be a promising MRI contrast agent.

To examine their in vivo MRI capabilities, the Fe_3O_4 @PDA-PEG-cRGD-DOX NPs were injected into the tail vein of nude mice, and 3.0-T MRI scans were performed before (0 h) and after (12 and 24 hrs) the injection. The in vivo MR imaging results (Figure 7D) showed that the *T*2-weighted MRI signal in the tumor tissue gradually decreased as the circulation time increased, especially after 24 hrs when the MRI signal in the tumor significantly decreased. These results showed that the Fe_3O_4@PDA-PEG-cRGD-DOX NPs could effectively target the tumor tissue, owing to active cRGD targeting and the EPR effect, and that they demonstrated improved MRI imaging contrast, which indicated they could be used for MRI-guided tumor treatment.

In vivo Pharmacokinetics Study

The pharmacokinetics behavior of DOX was studied in rats through the tail-vein injection of free DOX/Fe_3O_4 @PDA-PEG-cRGD-DOX NPs. The concentration of DOX in plasma at different times are shown in Figure 8. Compared with free DOX, the pharmacokinetic characteristics of Fe_3O_4@PDA-PEG-cRGD-DOX in vivo was significantly changed based on the pharmacokinetic parameters of the two groups as presented in Table 1. At the same dose, the distribution half-life time ($t_{1/2\alpha}$) and elimination half-life time ($t_{1/2\beta}$) of DOX in Fe_3O_4@PDA-PEG-cRGD-DOX group were significantly increased by 0.49 hrs and 5.92 hrs, respectively, compared with free DOX group. The clearance rate (CL) and elimination rate constant (K_{el}) values of free DOX group were 3.54 and 3.27 times as much as Fe_3O_4@PDA-PEG-cRGD-DOX group, respectively. The decreases of in vivo CL and K_{el} in Fe_3O_4@PDA-PEG-cRGD-DOX group might be due to the increased blood stability by escaping the reticular endothelial system (RES) and the sustained release of DOX from NPs. In addition, the mean retention time (MRT), area under the curve $(AUC)_{0-t}$ and $AUC_{0-\infty}$ values of Fe_3O_4 @PDA-PEG-cRGD-DOX group were significantly increased by 1.57, 3.60 and 3.49-fold, respectively, compared with free DOX group.

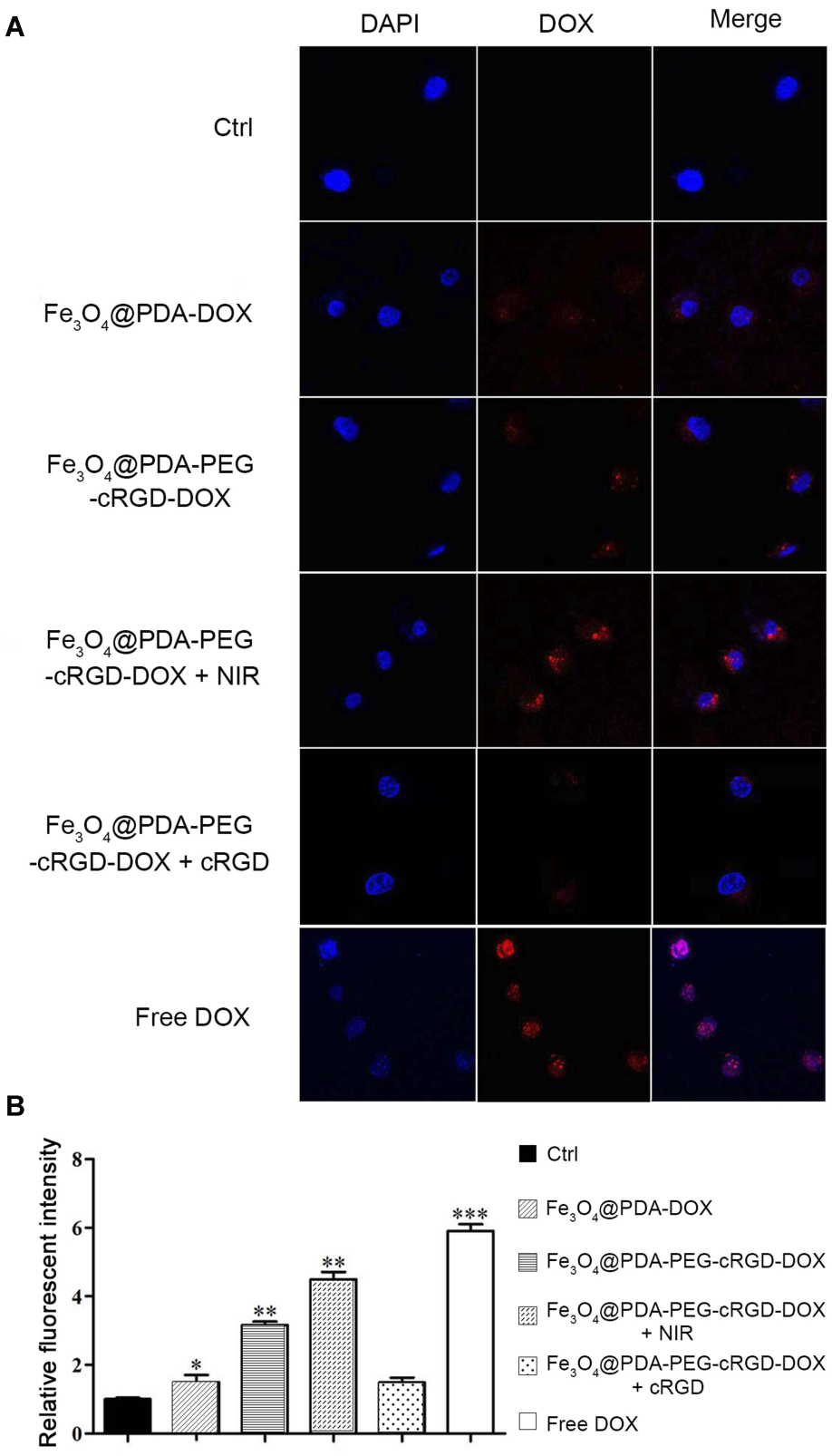

Figure 6 Cellular uptake. (**A**) Images of HCT-116 cells after a 2-h incubation with the Fe_3O_4@PDA-DOX NPs or Fe_3O_4@PDA-PEG-cRGD-DOX NPs exposed under NIR or not. (**B**) Relative fluorescent intensity in different groups. Observation was blue fluorescence DAPI nuclear staining (left column), red fluorescence from DOX encapsulated in the NPs (middle column), and the colocalization of DAPI and DOX (right column). Original magnification: 20×.

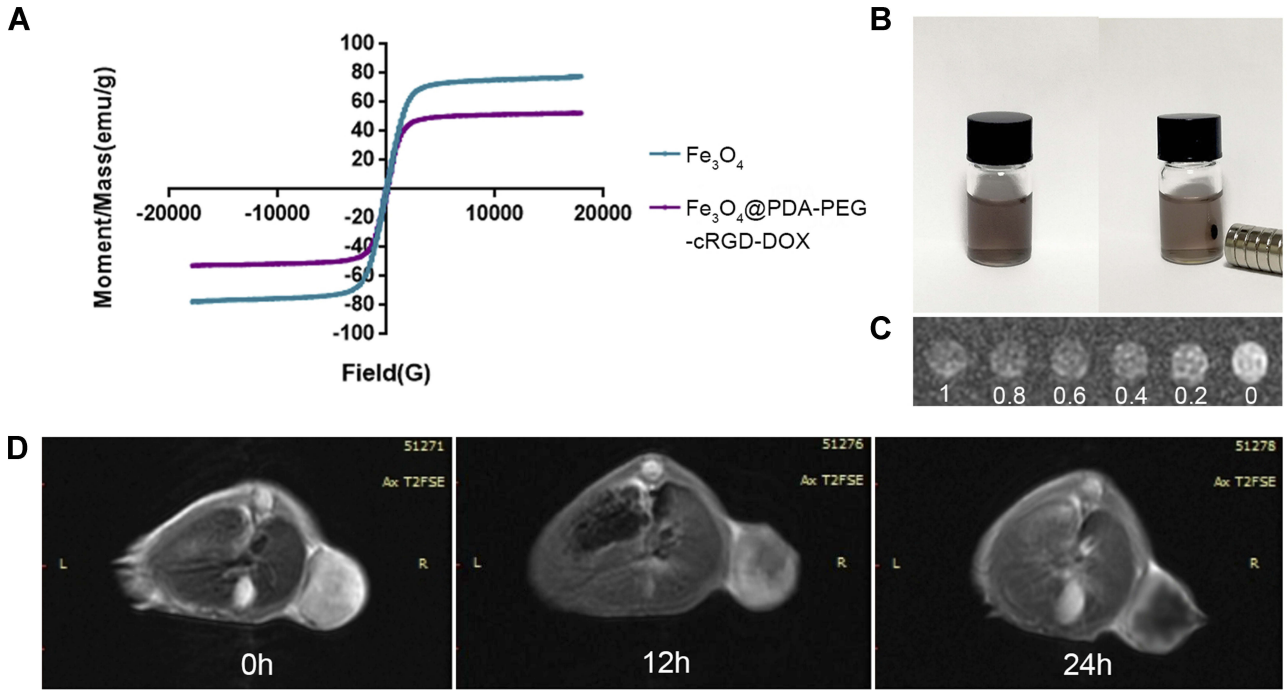

Figure 7 Hysteresis loop and magnetic properties in vivo and in vitro. (**A**) Magnetic hysteresis curves Fe_3O_4@PDA-PEG-cRGD-DOX at 300K. (**B**) Showed two bottles of the sample Fe_3O_4@PDA-DOX composite particles in the same concentration of the aqueous solution, in which the particles were well dispersed in water and attracted to the sidewall by a magnet. (**C**) Showed T2-weighted MRI photographs of the Fe_3O_4@PDA nanoparticles dispersed in water with different concentrations (0, 0.2, 0.4, 0.6, 0.8, 1.0 μg/mL). TR: 1100.0 ms; TE: 28.7 ms, field of view, 150 × 250 mm; and slice, 2.5 mm. (**D**) In vivo T2-weighted MRI images. TR: 1800.0 ms; TE: 43.2 ms, field of view, 50 × 90 mm; and slice, 2.5 mm.
Notes: T2-weighted MRI images of mice after intravenous injection with Fe_3O_4@PDA-PEG-cRGD-DOX NPs at 0, 12, and 24 hrs.

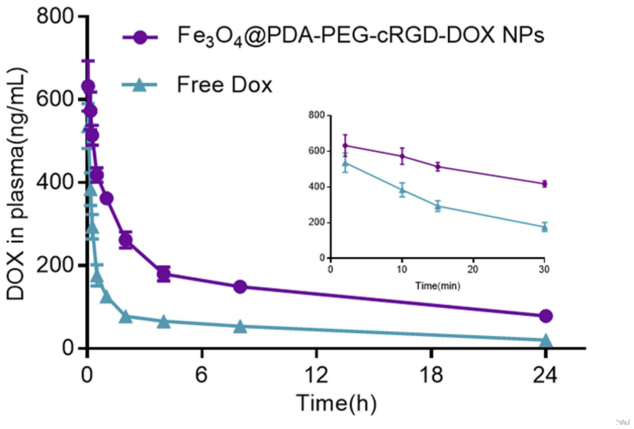

Figure 8 In vivo pharmacokinetics. The plasma concentration of DOX in two groups (n=3) of healthy SD rats treated with tail-vein injection of free DOX and Fe_3O_4@PDA-PEG-cRGD-DOX with doses of 1.5 mg/kg at different times.

The experimental results showed that DOX loading into Fe_3O_4@PDA-PEG-cRGD NPs could make the drug release slowly in a more stable and continuous way. Fe_3O_4@PDA-PEG-cRGD-DOX NPs extended the drug's circulation time, which could significantly reduce the DOX dose needed to achieve efficacy, thus reducing dose-dependent toxicity.

In vivo Therapeutic Effects

The antitumor effects of different nanoparticles under photothermal conditions were investigated in vivo. A xenograft model of nude mice with colon cancer was constructed, and the mice were randomly divided into eight groups (n = 6 per group): the normal saline group, pure NIR group, Fe_3O_4@PDA NP group, Fe_3O_4@PDA NP + NIR group, Fe_3O_4@PDA-DOX NP group, Fe_3O_4@PDA-DOX NP + NIR

Table 1 Pharmacokinetic Parameters of DOX and Fe_3O_4@PDA-PEG-cRGD-DOX After a Single Dosage Intravenous to Rat

Pharmacokinetic Parameters	DOX	Fe_3O_4 @PDA-PEG-cRGD DOX NP
$t_{1/2\alpha}$ (h)	0.23±0.01	0.72±0.04***
$t_{1/2\beta}$ (h)	11.18±1.46	17.10±0.76**
K_{el} (h^{-1})	0.36±0.03	0.11±0.01***
CL (mL/h)	242.70±45.08	68.53±7.10**
MRT (h)	14.58±1.91	22.84±1.15**
$AUC_{0\rightarrow\infty}$ (μg·h/mL)	1.58±0.27	5.51±0.57***
$AUC_{0\rightarrow t}$ (μg·h/mL)	1.45±0.25	5.23±0.52***

Notes: **P<0.01, ***P<0.001 versus free DOX treatment. Data were presented as mean ± SD (n=3).

group, Fe_3O_4@PDA-PEG-cRGD-DOX NP group, and Fe_3O_4@PDA-PEG-cRGD-DOX NP + NIR group (for those groups that underwent irradiation, in each case, the wavelength was 808 nm, power density was 1 W/cm^2, and the irradiation time was 5 mins). Figure 9A illustrates the animal experiments schematically. After the administration of the drug via a tail-vein injection, the NIR groups were treated with light the following day, and the tumors and body weights were subsequently measured every 4 days.

Figure 9B reveals rapid tumor growth in the control, pure NIR, and Fe_3O_4@PDA NP groups. In contrast, as shown in Figure 9B, tumor growth was inhibited in the Fe_3O_4@PDA-DOX NP group and Fe_3O_4@PDA NP + NIR group. This occurred because DOX itself had an antitumor effect, and the Fe_3O_4@PDA NPs could accumulate, to a certain extent, in the tumor tissue through passive targeting and inhibition of tumor growth under PTT. In addition, the Fe_3O_4@PDA-DOX NP + NIR group and Fe_3O_4@PDA-PEG-cRGD-DOX NP group displayed greater tumor inhibition effects. This was because the Fe_3O_4@PDA-DOX NP + NIR group received PTT along with DOX chemotherapy. The Fe_3O_4@PDA-PEG-cRGD-DOX NP group had a greater accumulation of DOX at the tumor sites and the chemotherapy effect of DOX was enhanced in this group through active targeting. Finally, the Fe_3O_4@PDA-PEG-cRGD-DOX NP + NIR group showed the best tumor inhibition effect among the groups because the these NPs had a long circulation time to enable the functioning of the EPR and active cRGD targeting effects, which facilitated the accumulation of larger amounts of this material in tumor tissues and maximized the synergistic effects of PTT and DOX chemotherapy.

The safety of nanomaterials is a critical factor affecting their in vivo application. The body-weight data of the nude mice (Figure 9C) showed that the body weights of the normal saline, pure NIR, and Fe_3O_4@PDA NP groups decreased slightly over the course of this experiment, possibly because the tumor sizes were sufficiently large to cause the emaciation of the nude mice. The weights of the mice in the other groups were stable, indicating that the nanomaterials had no obvious toxicity.

HE staining results (Figure 10A) showed that, compared with the control group, the heart, liver, spleen, lung, and kidney of the experimental groups exhibited no obvious inflammation or damage, indicating that the Fe_3O_4@PDA-PEG-cRGD-DOX NP probably did not cause systemic toxicity and had good biological safety. The H&E staining results for the tumor tissues of each group (Figure 10B) showed that the necrotic range in the Fe_3O_4@PDA NP, Fe_3O_4@PDA-DOX NP, and Fe_3O_4@PDA-PEG-cRGD-DOX groups gradually increased, and was greater than those in the control group. Furthermore, this phenomenon was more obvious in the

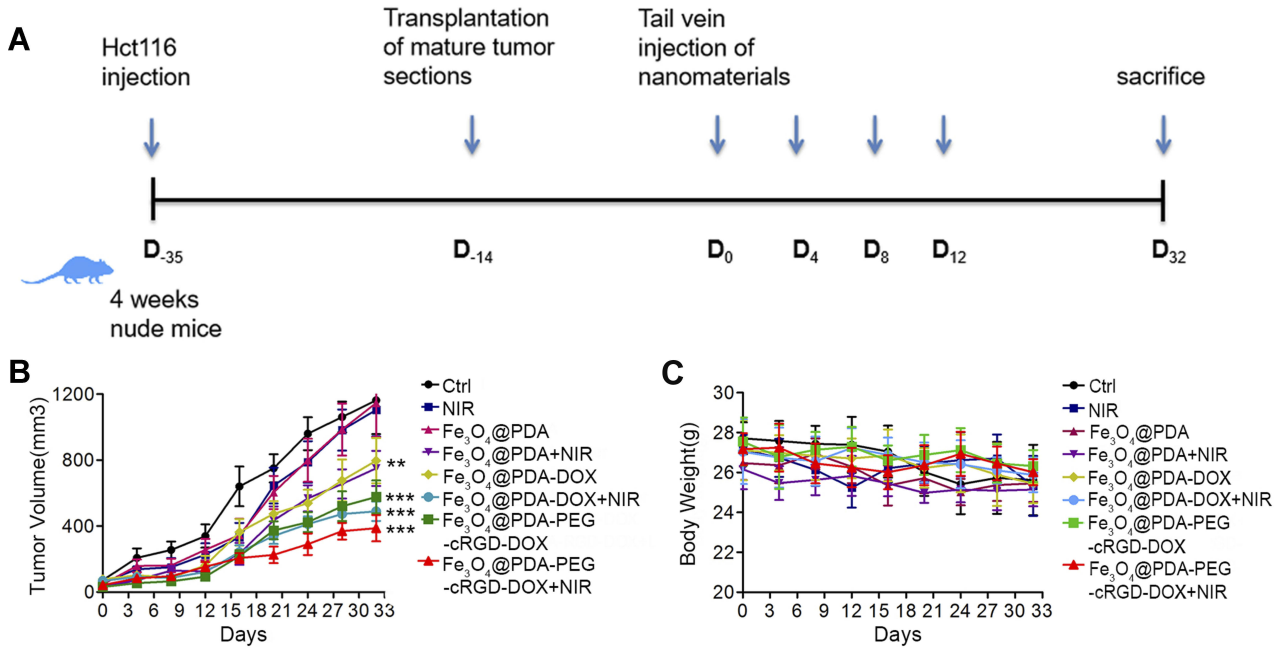

Figure 9 The antitumor efficiency was evaluated in the HCT-116 cancer-bearing mice. (**A**) Schematic illustration of the experimental protocol and tumor challenge. (**B**) Tumor volume change in HCT-116 subcutaneous tumor mice were monitored and analyzed using one-way ANOVA. (**C**) Mice in each group were implanted with subcutaneous tumor. After the tumor grew to an average of 5 mm, the bodyweight of the mice was measured every 4 days until death.

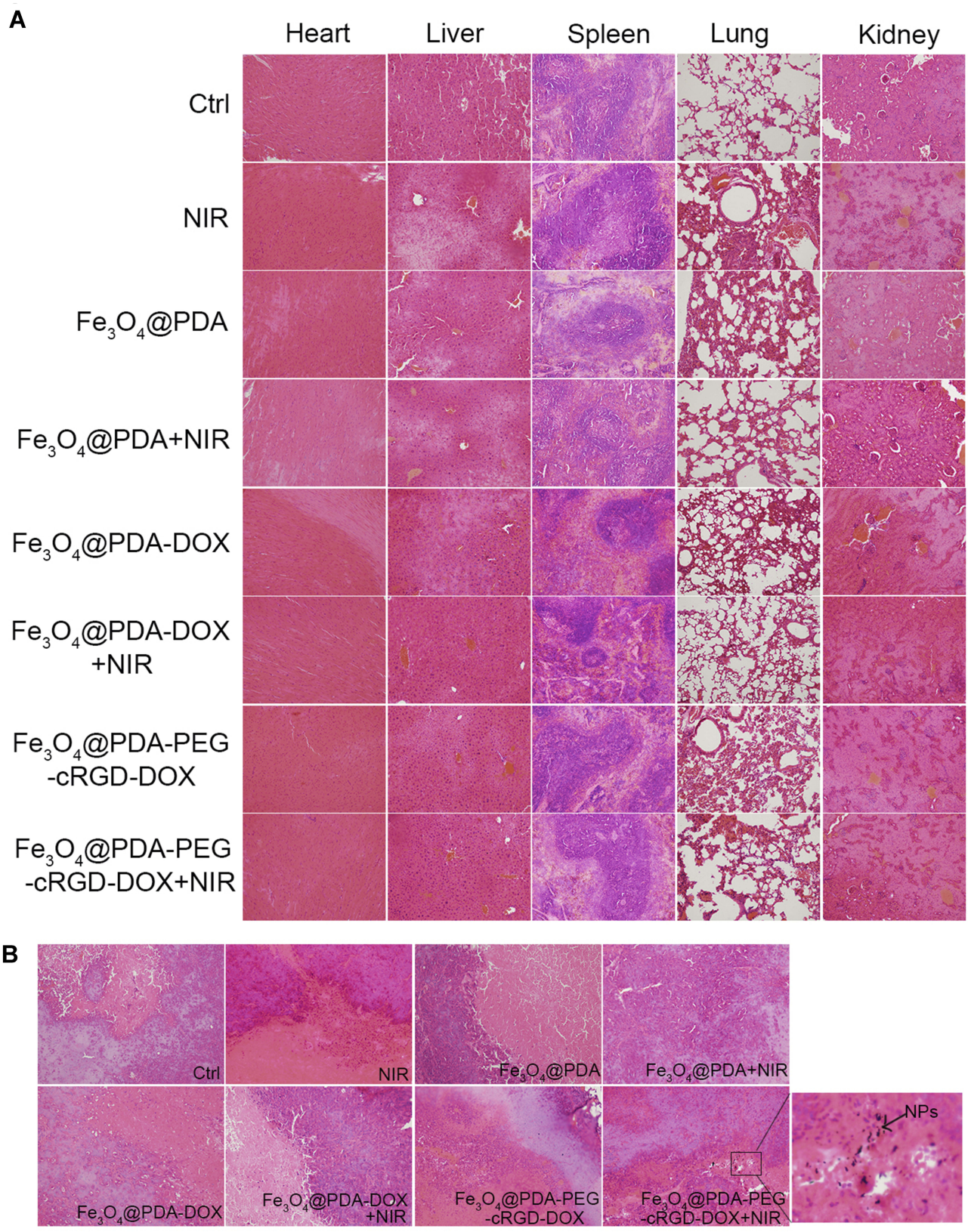

Figure 10 H&E staining of the organs (heart, liver, spleen, lung, and kidney) and tumors. (**A**) The hearts, livers, spleens, lungs and kidneys of the eight groups of tumor-bearing mice were taken out and sectioned for H&E staining. (**B**) Results of HE staining in tumor tissues of each group. Original magnification: 20×.

groups treated with NIR. At the same time, scattered brown and black nanoparticles were found in tumor sections 48 hrs after the Fe_3O_4@PDA-PEG-cRGD-DOX NP injection, which suggested that the nanomaterial could play a role in the long-term treatment of tumors.

Conclusion

We prepared multifunctional Fe_3O_4@PDA-PEG-cRGD-DOX NPs to integrate MRI diagnosis with photothermal therapy and chemotherapy. We demonstrated that this nanosystem has good biocompatibility and excellent photothermal conversion ability. DOX was adsorbed onto the surface of the nanoparticles via a π–π bond to facilitate its release under acidic and photothermal conditions. The NPs significantly suppressed the proliferation of HCT-116 cells in vitro and synergistically played a role in DOX chemotherapy and PTT. In vivo experiments showed that the NPs could effectively target tumor tissues, thanks to EPR and active targeting effects that they had good MRI contrast, and that they could significantly inhibit tumor growth under NIR irradiation.

In summary, the Fe_3O_4@PDA-PEG-cRGD-DOX NPs can be used as a potentially effective vector for the diagnosis of tumors and for combined chemotherapy and photothermal therapy.

Acknowledgment

This work was supported by the National Natural Science Foundation of China (grant nos. 81603502), Shanghai "Yiyuan new star" Funding Project for Distinguished Young Medical Talants Training and 3-Year Action Plan for Shanghai Municipal Chinese Medicine Development Project (No. ZY[2018-2020]-RCPY-2016).

Disclosure

The authors report no conflicts of interest in this work.

References

1. Chen W, Zheng R, Badde PD. Cancer statistics in China. *CA Cancer J Clin*. 2015;2:115–132.
2. Kuipers EJ, Grady WM, Lieberman D, et al. Colorectal cancer. *Nat Rev Dis Primers*. 2015;1:150–165. doi:10.1038/nrdp.2015.65
3. Modest DP, Pant S, Sartore-Bianchi A. Treatment sequencing in metastatic colorectal cancer. *Eur J Cancer*. 2019;109:70–83. doi:10.1016/j.ejca.2018.12.019
4. Clifford R, Govindarajah N, Parsons JL, et al. Systematic review of treatment intensification using novel agents for chemoradiotherapy in rectal cancer. *Br J Surg*. 2018;12:1553–1572. doi:10.1002/bjs.10993
5. Cousins A, Thompson SK, Wedding AB, et al. Clinical relevance of novel imaging technologies for sentinel lymph node identification and staging. *Biotechnol Adv*. 2014;32:269–279. doi:10.1016/j.biotechadv.2013.10.011
6. Kievit FM, Zhang MQ. Surface engineering of iron oxide nanoparticles for targeted cancer therapy. *Acc Chem Res*. 2011;10:853–862. doi:10.1021/ar2000277
7. Liu YJ, Bhattarai P, Dai ZF, et al. Photothermal therapy and photoacoustic imaging via nanotheranostics in fighting cancer. *Chem Soc Rev*. 2019;48(7):2053–2108.
8. Beik YJ, Abed Z, Ghoreishi FS, et al. Nanotechnology in hyperthermia cancer therapy: from fundamental principles to advanced plications. *J Control Release*. 2016;235:205–221. doi:10.1016/j.jconrel.2016.05.062
9. Zhu X, Feng W, Chang J, et al. Temperature-feedback upconversion nanocomposite for accurate photothermal therapy at facile temperature. *Nat Commun*. 2016;4:10437. doi:10.1038/ncomms10437
10. Liu YX, Jia Q, Guo QW, et al. pH-activated heat shock protein inhibition and radical generation enhanced NIR luminescence imaging-guided photothermal tumour ablation. *Int J Pharm*. 2019;566:40–45. doi:10.3923/ijp.2019.40.49
11. Gai S, Yang G, Yang P, et al. Charge convertibility and near infrared photon co-enhanced cisplatin chemotherapy based on upconversion nanoplatform. *Nano Today*. 2017;130:42–45.
12. Tahmasbi Rad A, Chen CW, Aresh WF, Xia Y, Lai PS, Nieh MP. Combinational effects of active targeting, shape, and enhanced permeability and retention for cancer theranostic nanocarriers. *ACS Appl Mater Interfaces*. 2019;11(11):10505–10519.
13. Bertrand N, Wu J, Xu X, Kamaly N, Farokhzad OC. cancer nanotechnology: the impact of passive and active targeting in the era of modern cancer biology. *Drug Delivery Rev*. 2014;66:22–25. doi:10.1016/j.addr.2013.11.009
14. Setyawati MI, Tay CY, Chia SL, et al. Titanium dioxide nanomaterials cause endothelial cell leakiness by disrupting the homophilic interaction of VE–cadherin. *Nat Commun*. 2013;4:1673. doi:10.1038/ncomms2655
15. Matsumura Y, Maeda H. A new concept for macromolecular therapeutics in cancer chemotherapy: mechanism of tumoritropic accumulation of proteins and the antitumor agent smancs. *Cancer Res*. 1986;46:6387–6392.
16. Riley RS, Day ES, Interdiscip W. Gold nanoparticle-mediated photothermal therapy: applications and opportunities for multimodal cancer treatment. *Wiley Interdiscip Rev Nanomed Nanobiotechnol*. 2017;9:1449–1458. doi:10.1002/wnan.1449
17. Zeng JY, Zhang MK, Peng MY, et al. Porphyrinic metal–organic frameworks coated gold nanorods as a versatile nanoplatform for combined photodynamic/photothermal/chemotheory of tumor. *Adv Funct Mater*. 2018;20:1705451. doi:10.1002/adfm.201705451
18. Guo Z, Zhu S, Yong Y, et al. Synthesis of BSA-coated BiOI@Bi2 S3 semiconductor heterojunction nanoparticles and their applications for radio/photodynamic/photothermal synergistic therapy of tumor. *Adv Mater*. 2017;20:1704136. doi:10.1002/adma.201704136
19. Xing Y, Zhang J, Chen F, et al. Mesoporous polydopamine nanoparticles with co-delivery function for overcoming multidrug resistance via synergistic chemo-photothermal therapy. *Nanoscale*. 2017;9:8781–8790. doi:10.1039/C7NR01857F
20. Xu X, Wang J, Wang Y, et al. Formation of graphene oxide-hybridized nanogels for combinative anticancer therapy. *Nanomedicine*. 2018;14:2387–2395. doi:10.1016/j.nano.2017.05.007
21. Liu Y, Zhi X, Yang M, et al. Tumor-triggered drug release from calcium carbonate-encapsulated gold nanostars for near-infrared photodynamic/photothermal combination antitumor therapy. *Theranostics*. 2017;7:1650–1662. doi:10.7150/thno.17602
22. Goodman AM, Neumann O, Norregaard K, Henderson L. Near-infrared remotely triggered drug-release strategies for cancer treatment. *Acad Sci U S A*. 2017;114:12419–12424. doi:10.1073/pnas.1713137114
23. Liu Y, Jia Q, Guo Q, et al. Simultaneously activating highly selective ratiometric MRI and synergistic therapy in response to intratumoral oxidability and acidity. *Biomaterials*. 2018;180:104–116. doi:10.1016/j.biomaterials.2018.07.025

24. Chu M, Shao Y, Peng J. Near-infrared laser light mediated cancer therapy by photothermal effect of Fe_3O_4 magnetic nanoparticles. *Biomaterials*. 2013;16:4078–4088. doi:10.1016/j.biomaterials.2013.01.086
25. Ao L, Wu C, Liu K. Polydopamine derivated hierarchical nanoplatform for efficient dual-modal imaging guided combination in vivo cancer therapy. *ACS Appl Mater Interfaces*. 2018;10:12544–12552. doi:10.1021/acsami.8b02973
26. Wang X, Zhang J, Wang Y. Multi-responsive photothermal-chemotherapy with drug-loaded melanin-like nanoparticles for synergetic tumor ablation. *Biomaterials*. 2015;81:114–124. doi:10.1016/j.biomaterials.2015.11.037
27. Liu YX, Guo QW, Zhu XJ, et al. Optimization of prussian blue coated $NaDyF_4$: x%Lu nanocomposites for multifunctional imaging-guided photothermal therapy. *Adv Funct Mater*. 2016;26:5120–5130. doi:10.1002/adfm.v26.28
28. Harisinghani MG, Barentsz J, Hahn PF. Noninvasive detection of clinically occult lymph-node metastases in prostate cancer. *N Engl J Med*. 2013;348:2491–2499. doi:10.1056/NEJMoa022749
29. Heilmaier C, Lutz AM, Bolog N, et al. Focal liver lesions: detection and characterization at double-contrast liver MR imaging with ferucarbotran and gadobutrol versus single-contrast liver MR imaging. *Radiology*. 2019;253:724–733. doi:10.1148/radiol.2533090161
30. Seeney CE. The emerging applications of magnetic nanovectors in nanomedicine. *Pharm Pat Anal*. 2015;4:285–304. doi:10.4155/ppa.15.17
31. Heilmaier C, Ruiz A, Gutiérrez L, et al. Biotransformation of magnetic nanoparticles as a function of coating in a rat model. *Nanoscale*. 2015;7:16321–16329. doi:10.1039/C5NR03780H
32. Kolosnjaj-Tabi J, Lartigue L, Javed Y, et al. Biotransformations of magnetic nanoparticles in the body. *Nano Today*. 2016;11:280–284. doi:10.1016/j.nantod.2015.10.001
33. Liu Y, Ai K, Liu J, et al. Dopamine-melanin colloidal nanospheres: an efficient near-infrared photothermal therapeutic agent for in vivo cancer therapy. *Adv Mater*. 2013;25:1353–1359. doi:10.1002/adma.v25.9
34. Hak-Sung J, Kyung-Jin C, Yeonee S. Polydopamine encapsulation of fluorescent nanodiamonds for biomedical applications. *Adv Funct Mater*. 2018;28:1801252. doi:10.1002/adfm.201801252
35. Barandov A, Bartelle BB, Gonzalez BA, et al. Membrane-permeble Mn(III) complexes for molecular magnetic resonance imaging of intracellular targets. *J Am Chem Soc*. 2016;138:5483–5486. doi:10.1021/jacs.5b13337
36. Teo PY, Cheng W, Hedrick JL, et al. Co-delivery of drugs and plasmid DNA for cancer therapy. *Adv Drug Deliv Rev*. 2016;98:41–63. doi:10.1016/j.addr.2015.10.014
37. Zheng R, Wang S, Tian Y, et al. Polydopamine-coated magnetic composite particles with enhanced photothermal effect. *CS Appl Mater Interfaces*. 2015;7:15876–15884. doi:10.1021/acsami.5b03201
38. Cao L, Du P, Jiang S, et al. Enhancement of antitumor properties of TRAIL by targeted delivery to the tumor neovasculature. *Mol Cancer Ther*. 2008;7:851–861. doi:10.1158/1535-7163.MCT-07-0533
39. Zhi S, Lin Y, Zhang X, et al. Cyclic RGD peptide-modified liposomal drug delivery system for targeted oral apatinib administration: enhanced cellular uptake and improved therapeutic effects. *Int J Nanomedicine*. 2017;12:1941–1958. doi:10.2147/IJN.S125573
40. Koivunen E, Wang B, Ruoslahti E. Phage libraries displaying cyclic peptides with different ring sizes: ligand specificities of the RGD-directed integrins. *Biotechnology*. 1995;13:265–270. doi:10.1038/nbt0395-265
41. Assa-Munt N 1, Jia X, Laakkonen P, et al. Solution structures and integrin binding activities of an RGD peptide with two isomers. *Biochemistry*. 2001;40:2373–2378. doi:10.1021/bi002101f
42. Burkhart DJ, Kalet BT, Coleman MP. Doxorubicin-formaldehyde conjugates targeting alphavbeta3 integrin. *Mol Cancer Ther*. 2004;3:1593–1604.
43. Kolhar P, Kotamraju VR, Hikita ST, et al. Synthetic surfaces for human embryonic stem cell culture. *J Biotechnol*. 2010;146:143–146. doi:10.1016/j.jbiotec.2010.01.016